Journal of Alloys and Compounds 908 (2022) 164604

Contents lists available at ScienceDirect

Journal of Alloys and Compounds

journal homepage: www.elsevier.com/locate/jalcom

Zr-based quaternary half-Heusler alloy systems $ZrNi_mX_{0.5}Sb_{1.5-m}$ (X=Fe/In): Studies on phase evolution, crystal structures and electronic properties

Dipanjan kumar[a], Surafel Shiferaw Legese[a,b], Shriparna Mukherjee[a,e], Olu Emmanuel Femi[b], Ravishankar Narayanan[c], Kamanio Chattopadhyay[a,d,*]

[a] Interdisciplinary Centre for Energy Research, Indian Institute of Science, Bangalore 560012, India
[b] Faculty of Materials Science and Engineering, Jimma Institute of Technology, Jimma, Ethiopia
[c] Materials Research Centre, Indian Institute of Science, Bangalore 560012, India
[d] Department of Materials Engineering, Indian Institute of Science, Bangalore 560012, India
[e] Department of Chemistry, University of Reading, Reading RG6 6DX, United Kingdom

ARTICLE INFO

Article history:
Received 27 November 2021
Received in revised form 17 February 2022
Accepted 14 March 2022
Available online 16 March 2022

Keywords:
Half-Heusler alloys
Quaternary
Disordered
TEM
Aliovalent substitutions
Semiconductor

ABSTRACT

Half Heusler(hH) compounds have demonstrated exceptional capability in a wide range of functional applications as semiconductors. Although there are theoretical predictions about newer compounds and their thermodynamic stability, experimental validation is often missing. In this study, we report two quaternary multicomponent Zr-based hH alloy systems, namely $ZrNi_{0.5}Fe_{0.5}Sb$ and $ZrNiIn_{0.5}Sb_{0.5}$, designed by combining 19 and 17 VEC (valence electron count) alloy systems. The structural features, including the crystal structures and compositions, were established using multiple techniques like X-ray diffraction, scanning and transmission electron microscopy. Both these systems crystallized in signature hH cubic structure ($F\bar{4}3m$) having lattice parameters 0.6091 nm and 0.6104 nm, respectively. The measurement of Seebeck coefficients over a wide temperature range showed p-to n-type semiconductor transition in $ZrNi_{0.5}Fe_{0.5}Sb$ at around 888 K due to bipolar conduction. Subsequently, the partial substitution of Co for Fe sites ($ZnNi_{0.5}Fe_{0.3}Co_{0.2}Sb$) completely suppressed the bipolar conductivity, making it a n-type semiconductor and increased the absolute value of Seebeck coefficient, by an order of magnitude, to − 133μV/K. The alloy $ZrNiIn_{0.5}Sb_{0.5}$ showed n-type semiconductor behavior throughout the measurement temperature range. This study conducts an in-depth examination of the microstructural phase evolution, chemical environment of the elements forming the novel hH phase and demonstrates the tunability of electronic properties through aliovalent substitutions at various lattice sites.

1. Introduction

Half-Heusler (hH) alloys are an emerging group of materials with a wide range of applications such as spintronics [1–3], topological insulators, [4,5] and, in the green energy-related fields of solar cells [6–8] or thermoelectrics (TEs) [9,10]. The cause of these versatile multifunctional applications from the same class of materials is due to the unique cubic crystal structure (Space group no. 216, $F\bar{4}3m$, $C1_b$) that can accommodate various elements. The structure of a ternary equiatomic hH crystal XYZ can be viewed as three interpenetrating FCC lattices (hence, stoichiometry 1:1:1) occupied by different kinds of atoms [11]. It provides the flexibility of substituting atoms at different lattice sites by changing the chemical composition enabling a wide combinatorial space of ternary compounds. Consequently, the band gaps can be tuned in a wide range (0–4 eV) to optimize electronic, optical, and magnetic properties. It is widely acknowledged that alloys with 18 valence electron count (VEC) are stable semiconductors such that all of their bonding electronic states are filled, while all antibonding states are unfilled [12,13]. This VEC 18 criterion has been profusely employed for designing as well as predicting newer hH compounds [14,15]. Subsequently, two major designing strategies can be identified in the recent development of newer hH compounds. First, adjusting the chemical stoichiometry of ternary systems (having 17 and 19 VECs) such that the effective VEC comes closer to 18. These off-

* Corresponding author at: Department of Materials Engineering, Indian Institute of Science, Bangalore 560012, India.
E-mail address: kamanio@iisc.ac.in (K. Chattopadhyay).

https://doi.org/10.1016/j.jallcom.2022.164604
0925-8388/

stoichiometric compounds are called defective half Heuslers owing to the presence of large point defects like vacancies. $Nb_{0.8\pm x}FeSb$, and $TiFe_{1.5\pm x}Sb$ from NbCoSb [16] (19 VEC) and TiFeSb [17] (17 VEC) ternary systems, respectively, are the classical examples of these defective hHs. Theoretical studies based on first-principle calculations further predicted 16 newer defective hHs [18–22]. However, most of these ternary phases contain rare or precious elements that preclude any practical functional applications. Second, fulfilling the valence balance criterion (18 VEC) through a combination of 19 and 17 VEC systems. Anand et al.[23] explored such possibility theoretically and predicted a large phase space for the 131 quaternary hH crystals. This relatively newer strategy was based on the premise that such phases already existed in the early report of Skolozdra et al.[24], who reported cubic hH quaternary compounds ($Sc_{0.5}Nb_{0.5}FeSb$, $ZrNiIn_{0.5}Sb_{0.5}$, $HfNiIn_{0.5}Sb_{0.5}$). These compounds can be thought of as the combination of two such 17 and 19 VEC systems. However, the electronic properties of such compounds were not yet measured. To assess and extend the applicability of this strategy, we synthesized three Zr-based multicomponent alloy systems and investigated their microstructural, crystallographic, and electronic properties.

The purpose of this paper is two-fold. First, to explore new Zr-based half Heusler alloy systems that are designed to achieve a VEC of 18, synthesized by mixing ternary alloys of 17 and 19 VECs. The ternary system ZrNiSb having 19 VEC, is alloyed with 17 VEC systems of ZrFeSb and ZrNiIn such that the quaternary alloy stoichiometries can be conveniently expressed as $ZrNi_mX_{0.5}Sb_{1.5-m}$ (X = Fe, m=0.5; X=In, m=1). While transition elements Fe and Ni both occupy Y elemental site [Wyckoff site 4c (1/4,1/4,1/4)] in $ZrNi_{0.5}Fe_{0.5}Sb$ system, p-block heavier elements In and Sb both occupy Z elemental site [Wyckoff site 4b (1/2,1/2,1/2)] in $ZrNiSb_{0.5}In_{0.5}$, respectively, of the cubic hH lattice (space group $F\bar{4}3m$). Second, to investigate the phase stability and electronic properties of the achieved 18 VEC $ZrNi_{0.5}Fe_{0.5}Sb$ quaternary hH phase when alloyed with another ternary hH ZrCoSb system having 18 VEC. The same occupancy site [Wyckoff position 4c (1/4,1/4,1/4)] of Ni and Fe in $ZrNi_{0.5}Fe_{0.5}Sb$ lattice and Co in ZrCoSb lattice along with similar atomic sizes of these transition elements make ZrCoSb system suitable choice for alloying in the quaternary hH phase.

2. Experimental details

2.1. Sample preparation

Stoichiometric amounts of elements with 4 N purity were used for the synthesis of the alloys. Ingots (approximately 10 g) of desired compositions were prepared through conventional arc melting on a water-cooled copper heath under an inert gas atmosphere (Ar, 5 N). Prior melting, the chambar was pumped to vacuum (< 10^{-5}mbar) and purged with Ar. These steps were repeated three times to remove any contaminating gases. Additionally, the titanium sponge was used as gettering material to reduce oxygen contamination. The initial melted buttons were repeatedly re-melted after flipping the buttons several times to ensure homogenized ingot. Samples were then sealed in quartz ampoules under vacuum (< 10^{-5}mbar) and heat-treated at 900 °C for 7–9 days.

2.2. Sample characterization

The annealed samples were sectioned by Isomet slow speed cutter for various characterizations and measurement. For SEM and EPMA Characterizations, samples were embedded in epoxy resin and polished following the standard metallographic procedures using SiC grit papers from P800 to P4000 numbers. Final cloth polishing was carried out using 0.05 µm colloidal silica suspension. The microstructures of the phases were examined by scanning electron microscope (SEM, JEOL IT 300). Composition analysis was carried out using a Electron Probe Microanalyzer (EPMA, JEOL JXA-8530 F) equipped with a field-emission source. For overall alloy compositions, analysis was carried out using by EDS detector (area count) from a minimum of five different representative locations. The quantitative analysis of the composition of the local phases were conducted employing wavelength dispersive spectroscopy (WDS). Standard deviations on a minimum of five points measured per phase were less than ± 1 mass%. The structures of the phases present in the samples were investigated by powder X-ray diffraction with a Cu Kα radiation source (XRD, PANalytical X′pert PRO diffractometer). Quantitative Rietveld refinement protocol was used to determine the atom sites and lattice parameters employing the program FULLPROF. Detailed crystallographic and microstructural analysis was carried out using transmission electron microscopy (TEM, FEI Tecnai G2 T20 S-Twin). The TEM samples were prepared using a focused dual ion beam microscope (FIB, FEI Helios NanoLAB 600i) operating at 30 kV with final thinning at 5 kV. The selected–area diffraction patterns from the phases were indexed using JEMS software. For the measurement of the Seebeck coefficient and electrical resistivity, cuboidal bars of approximately 3 mm × 3 mm × 11 mm dimensions were directly cut from the ingots. The measurements were carried out in the ULVAC ZEM-3 system in the temperature range of 300–1000 K. The respective errors in the measurement of electrical resistivity and Seebeck coefficient are 10% and 7%, respectively.

3. Results and discussion

3.1. Microstructure and phase identification

The nominal compositions of all the alloys are given in Table 1 along with the nomenclature, which will be used henceforth to address the alloys. Fig. 1(a)-(c) show scanning electron micrographs in the backscattered electron mode of the annealed samples. Since cast ingots were used for heat treatment, voids are observed inside the grains, at triple points corners and grain boundaries of annealed samples shown by dashed red circles. The polycrystalline single phase can be observed with average composition ~ $ZrNi_{0.5}Fe_{0.5}Sb$ (Fig. 1a). Due to the valency balance requirement of 18 electrons for phase stability of hH alloys, $ZrNi_{0.5}Fe_{0.5}Sb$ can be thought of as an alloy mixture of 17 electron ZrFeSb and 19 electron ZrNiSb system. The off-stoichiometric composition (having VEC 18) of these 17-

Table 1
Compositional analysis of phases obtained in different alloy systems after annealing employing wavelength dispersive spectroscopy (WDS). Actual chemical formulae and VEC are computed from the measured composition of half Heusler phases.

Sample	Targeted Formulae	Targeted VEC	Phases	Calculated Formulae	Measured Composition (at%)						Obtained VEC (hH phase)
					Zr	Ni	Co	Fe	Sb	In	
ZNFS	$ZrNi_{0.5}Fe_{0.5}Sb$	18	hH	$Zr_{0.98}Ni_{0.48}Fe_{0.48}Sb_{0.99}$	32.8 ± 0.8	16.1 ± 0.2		15.9 ± 0.4	33.2 ± 0.5		17.7
ZNFS-Co	$ZrNi_{0.48}Fe_{0.3}Co_{0.2}Sb$	18	hH	$Zr_{0.99}Ni_{0.49}Fe_{0.3}Co_{0.2}Sb_{1.01}$	33.1 ± 0.2	16.2 ± 0.1	6.8 ± 0.1	10 ± 0.2	33.8 ± 0.8		18.1
ZNIS	$ZrNiIn_{0.5}Sb_{0.5}$	18	hH	$Zr_{0.98}Ni_{0.97}Sb_{0.52}In_{0.47}$	32.8 ± 0.7	32.4 ± 0.3			17.2 ± 0.4	15.6 ± 1.0	17.6
			μ_1	$ZrNi_2In$	25 ± 0.1	49.5 ± 0.4				25.1 ± 0.6	
			μ_2	$ZrNi_{0.78}Sb_{1-x}In_x$	35.9 ± 0.1	28.4 ± 0.2			32.4 ± 1.2	3.25 ± 0.6	

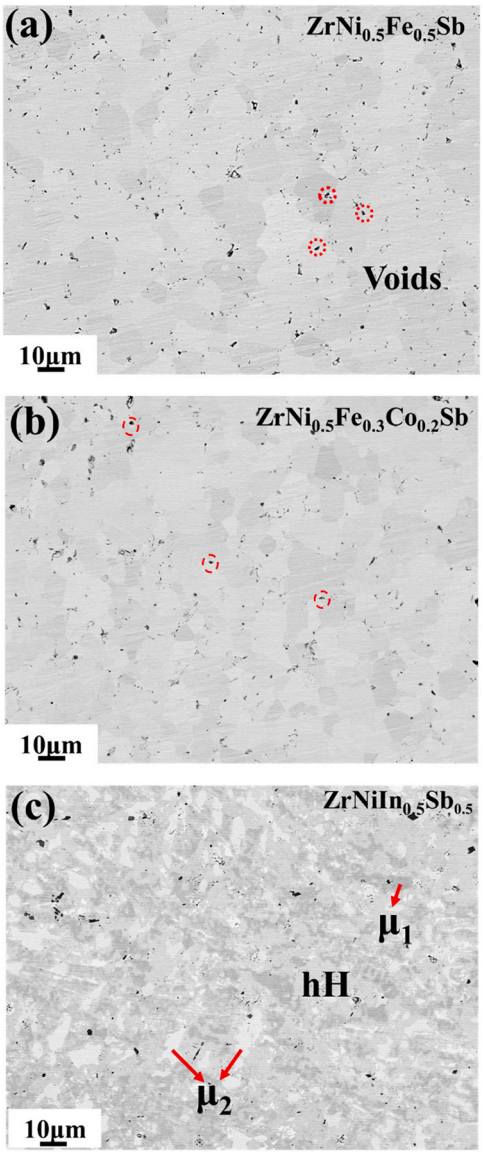

Fig. 1. BSE micrographs showing annealed microstructures of (a) ZNFS; (b) ZNFS-Co and (c) ZNIS alloys.

electron and 19-electron hH compositions would have been $ZrFe_{1+x}Sb$ and $Zr_{1-x}NiSb$. In the recently discovered Ti-based system [23,25], the analogous off-stoichiometric alloys; $TiFe_{1+x}Sb$ and $Ti_{1-x}NiSb$ [26–28] have been experimentally synthesized and their physical properties reported. However, for the present quaternary Zr-based hH alloy, related ternary Zr-based compositions have not been reported yet. Therefore, synthesis of $Zr_{1-x}NiSb$ ($Zr_{0.75}NiSb$, VEC 18) was also attempted. Quantitative analysis showed the presence of two phases with composition $Zr_3Ni_3Sb_4$ and $ZrNi_2Sb$ for this composition (Fig. S1 in supplementary information). This is consistent with the report by Romaka et. al [29] where the Zr-deficient side of compositional point ZrNiSb (1:1:1) is characterized by pseudo-binary phase field of $Zr_3Ni_3Sb_4$ and $ZrNi_2Sb$. For the case of $ZrFe_{1+x}Sb$, the phase is absent in the available Zr-Fe-Sb ternary diagram. Melnyk et al. [30] have reported three ternary compounds of $ZrFe_{1-x}Sb$, $Zr_6Fe_{1-x}Sb_{2+x}$, and $Zr_5Fe_{0.44}Sb_{2.56}$ in the Zr-Fe-Sb system while attempts by Kleinke and Felser [31] to synthesize Fe-rich ternary compound by overcompensation Fe did not succeed. Hence no attempt of synthesizing $ZrFe_{1+x}Sb$ was tried. In Co substituted ZNFS alloy (Fig. 1b), polycrystalline grains of hH single phase can be observed after annealing, having an average composition of $Zr_{33.1}Ni_{16.2}Fe_{10}Co_{6.8}Sb_{33.8}$. This quinary phase can be interpreted as an alloy mixture of ZrNiSb, ZrFeSb, and ZrCoSb ternary systems. ZrCoSb is an established ternary 18 VEC hH alloy whose crystal structure and properties are well studied [32,33]. Therefore, part Fe substitution with Co can be deduced as replacing 17 VEC ZrNiSb system with 18 VEC ZrCoSb system, thereby bringing the overall VEC closer to 18 and stabilizing this Co containing quinary phase. Fig. 1(c) show micrographs of annealed $ZrNiIn_{0.5}Sb_{0.5}$ (ZNIS) sample containing multiple phases, the compositions of which are given in Table 1. It was noted that the measured bulk alloy composition contained less amount of In than the stoichiometric amount taken before melting. This composition deviation is attributed to loss of In (vapor pressure of In melt increases rapidly above 1000 °C (0.05 mbar) to 11 mbar at 1400 °C) [34] during arc melting. However, the hH $ZrNiIn_{0.5}Sb_{0.5}$ phase is still the majority phase having a volume fraction ~65% coexisting with a darker Ni-rich $ZrNi_2In$ phase (denoted by μ_1) and a ternary μ_2 phase with volume fractions of ~21% and ~14% respectively (calculated through X-ray diffraction analysis). Minor amounts of InSb were also found in isolated regions. The ternary phase μ_2 ($ZrNi_{0.78}Sb_{1-x}In_x$) is In-deficient while enriched with Sb. No literature has been reported on this phase or any phase closer to this composition in Zr-Ni-Sb ternary system. The two ternary components that can lead to fulfilling the 18 VEC requirement in the alloy ZNIS are ZrNiSb and ZrNiIn. Three ternary compounds have been reported in the Zr-Ni-In system; $ZrNi_2In$ [35], Zr_2Ni_2In [36], and Zr_2NiIn_5 [37]. Based on the phase diagrams from the Open Quantum Materials Database, [38,39] ZrNiIn is thermodynamically unstable and decomposes into $Zr_2NiIn_5 + Zr_2Ni_2In$ and $ZrNi_2In$. Off-stoichiometric compositions crystallizing in hH crystal structure in ZrNiIn ternary system comparable to those like in TiFeSb are not yet reported.

Table 1 shows the experimental VEC values calculated from the average composition of hH phases obtained in these alloy systems. The computed values are close to the targeted 18 VEC for all the hH phases. Such small variations occur due to compositional changes occurring during arc-melting of elements which have large differences in their melting points. These minor VEC deviations however, indicates the availability of phase space in which the hH phases are thermodynamically stable. This is advantageous for tuning and optimizing carrier concentrations. A similar strategy of moving slightly away from 18 VEC to optimize semiconducting transport properties has already been reported in ternary hHs such ZrNiSn, $Nb_{0.8}CoSb$ [40,41]. The substitution of Fe with Co in ZNFS-Co leads to an additional valence electron contribution in the hH phase. This resulted in an increase in VEC of ZNFS-Co phase.

3.2. Crystal structure analysis

XRD powder patterns of the annealed alloy ZNFS, ZNFS-Co, and ZNIS are shown in Fig. 2(a) that corresponds to the typical cubic half-Heusler(hH) crystal structure (Space group $F\bar{4}3m$, C1b) with characteristic (111) and (220) reflections. Trace amount of the secondary FeSb phase can also be identified in the pattern of ZNFS. Rietveld refinements were performed for all three annealed alloys using a structural model (Space group $F\bar{4}3m$). Atomic positions of Zr and Sb were fixed at Wyckoff sites 4a and 4b, respectively. It has been reported earlier that hH alloys show different kinds of anti-site defects involving elements at Wyckoff positions 4a, 4b, 4c and 4d [12]. The presence of such defects are reflected in the change/absence of specific X-ray peak intensities. Since, the aliovalent substitution of Ni with Fe has been carried out in $ZrNi_{0.5}Fe_{0.5}Sb$ system at site 4c, possibilities of such anti-site defects were examined. The most commonly occurring defect in such cases is the non-stoichiometric distribution of elements at sites 4c occupying some vacant 4d sites as has been reported in the case of ternary hH ZrNiSn [42–46]. Simulated X-ray patterns of Ni and Fe occupying 4c and 4d sites

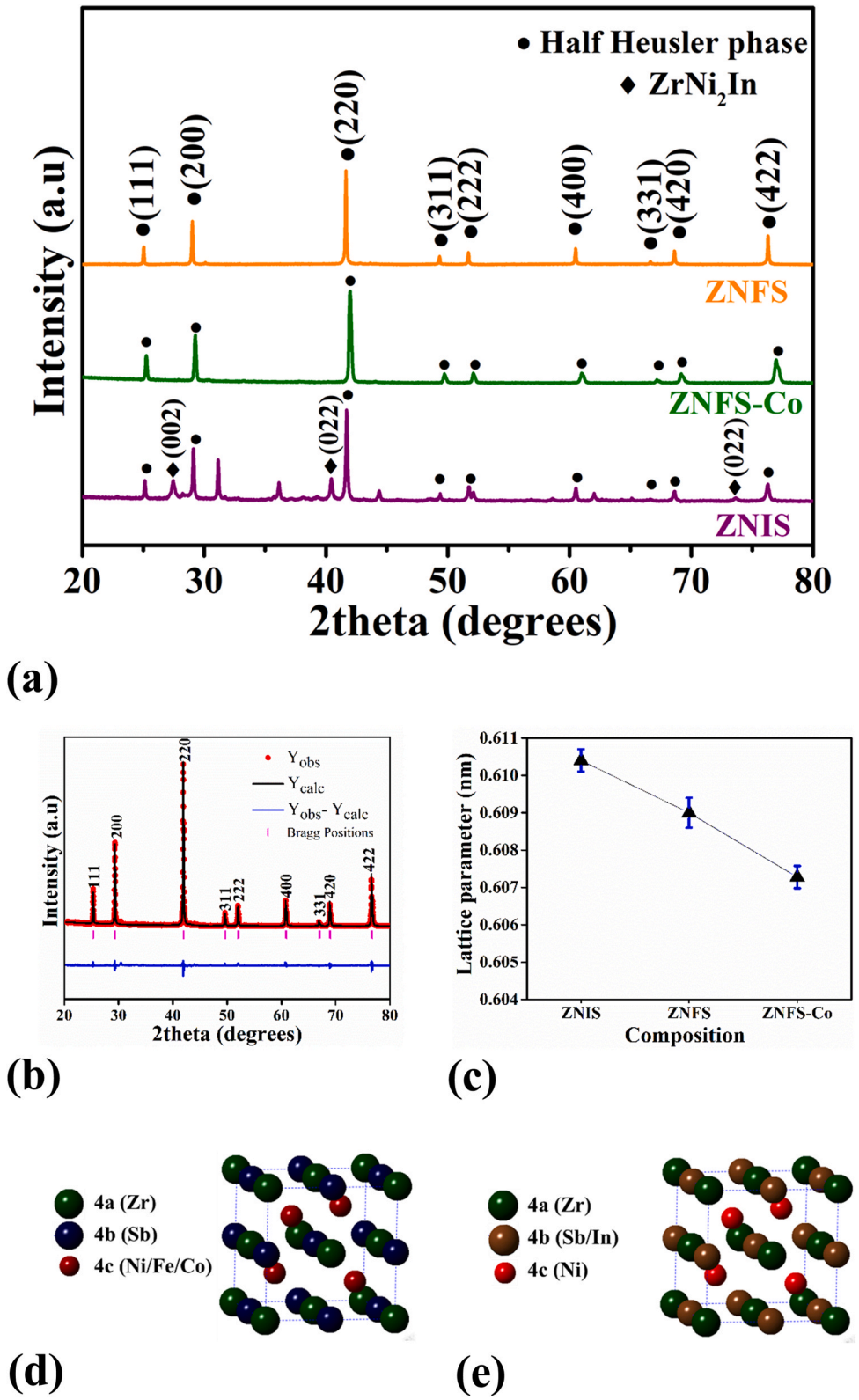

Fig. 2. (a) Powder XRD pattern of annealed ZNFS, ZNFS-Co and ZNIS alloys. (b) Reitveld refinement of $ZrNi_{0.5}Fe_{0.5}Sb$ (ZNFS) half Heusler phase. (chi^2 =2.11; R_{bragg} =5.07) (c) Lattice parameter comparison of various Half Heusler phases, Schematic of atomic structure of (d) ZNFS, ZNFS-Co and (e) ZNIS half Heuslers.

showed significantly higher ratios of (I_{200}) / (I_{111}) (refer to supplementary information, Fig. S2) which is consistent with the patterns generated for various atomic disorder [12]. Therefore, in absence of any change in peak intensity ratios (signature of anti-site defects), it was concluded that Ni and Fe both occupied 4c site. The final refinement is shown in Fig. 2(b). The lattice parameter was found to be 6.091 Å. In the case of ZNFS-Co alloy, similar possibilities for various occupancies of Co at different Wyckoff sites were also investigated. The refinement showed Co occupying 4c Wyckoff site substituting Fe and lattice parameter was found to be 6.071 Å. The

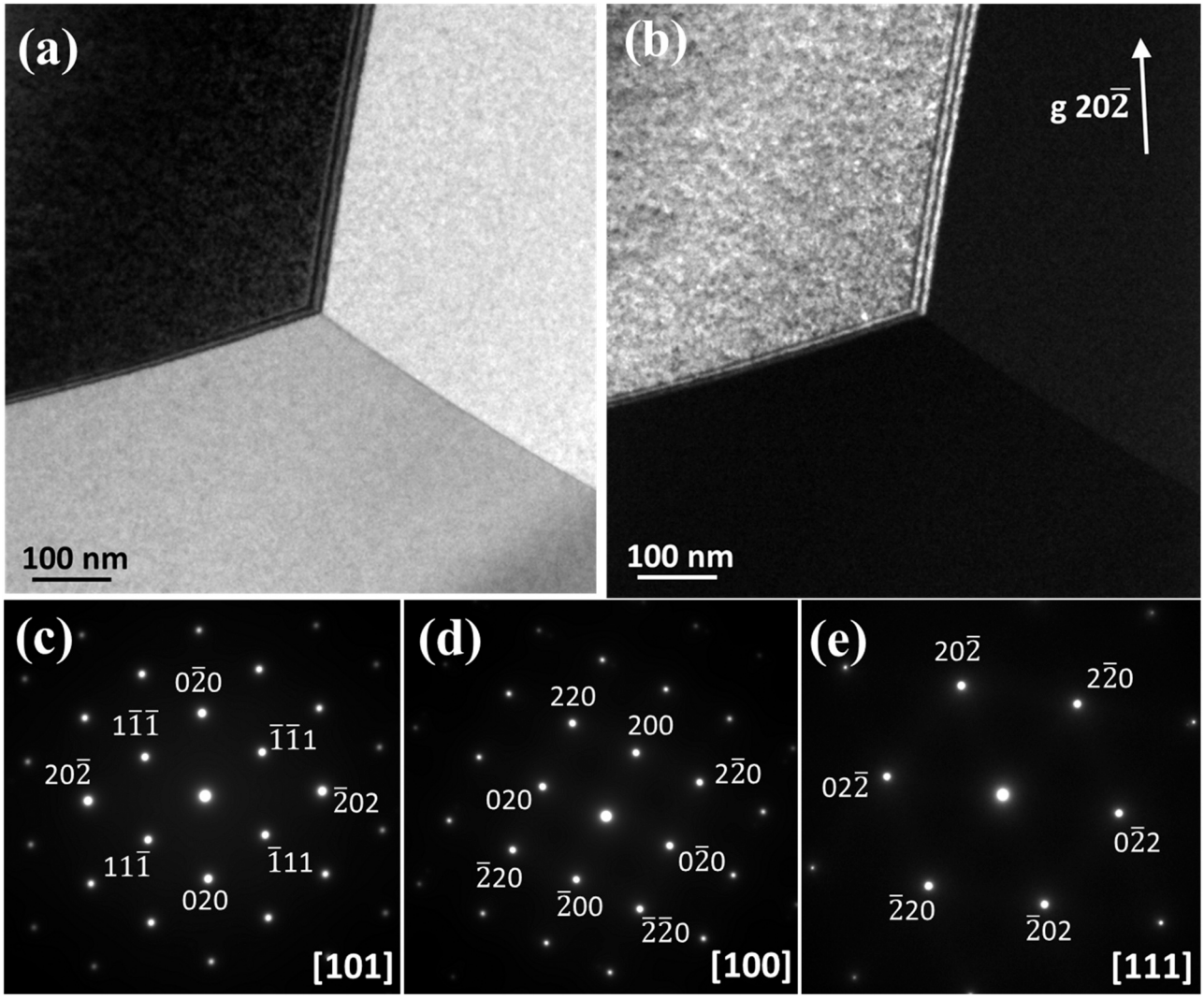

Fig. 3. (a) TEM BF image showing grain boundary triple junction of $ZrNi_{0.5}Fe_{0.5}Sb$ hH phase, (b) DF image formed under two-beam condition using (20$\bar{2}$) reflection of [101] zone axis direction. Major zone axis patterns indexed to (c) [101], (d) [100], and [111] directions.

absence of any superlattice peaks rules out the possibility of Ni/Fe/Co ordering. The schematic of the atomic arrangement of $ZrNi_{0.5}Fe_{0.5}Sb$ and ZNFS-Co is shown in Fig. 2(d). In the case of $ZrNiIn_{0.5}Sb_{0.5}$ (ZNIS) alloy with aliovalent substitution of Sb with In, the strongest reflections of the patterns can be indexed in terms of a cubic half-Heusler phase together with a phase $ZrNi_2In$. $ZrNi_2In$ has been previously reported to have a full-Heusler $L2_1$ crystal structure having Space group no. 225($Fm\bar{3}m$) [35]. Besides, the pattern exhibits few additional peaks which could not be indexed. These reflections most likely originated from the μ_2 phase since the volume fraction of the binary InSb phase is very low and unlikely to be detected by the powder X-ray technique. In Reitveld refinement of the hH phase, the best fit was obtained with positions of Zr and Ni fixed at Wyckoff sites 4a and 4c, respectively. Sb and In both were fixed at 4b site. Schematic of the atomic arrangement of $ZrNiIn_{0.5}Sb_{0.5}$ is shown in Fig. 2(e). The lattice parameters were calculated to be 6.104 Å for $ZrNiIn_{0.5}Sb_{0.5}$ phase and 6.286 Å for $ZrNi_2In$ phase. The observed lattice parameter for $ZrNi_2In$ phase is in good agreement with the reported value of 6.288 Å [47]. The variation of lattice parameters of these various hH phases is shown in Fig. 2(c).

Fig. 3(a) shows the bright-field TEM image of a triple point grain boundary junction of hH phase having ZNFS composition. The dark field image was formed under two-beam condition using (20$\bar{2}$) reflection of [101] zone axis direction of hH phase shown in Fig. 3(b). Additional major zone axis patterns were also gathered from this phase and can be indexed in terms of [001] and [111]. These diffraction patterns are shown in Fig. 3(c)-(f). Similar TEM investigations were also performed on hH phases from the other two alloys and are shown in the supplementary information (refer to supplementary information, Figs. S3-10). These electron diffraction patterns further confirm the cubic nature of hH phases formed in various alloy compositions. Additionally, no superlattice spots were observed in any of the major zone axes patterns confirming the absence of long-range ordering arising out of aliovalent substitutions carried out at various lattice sites. A common, occurring feature observed in all BF and DF images is the observation of contrast fringes along the grain boundaries. Such features occur in images where an inclined grain boundary is imaged under the dynamical two-beam condition in one grain and kinematical in the other [48].

3.3. Electronic properties

To determine the semiconducting type of these alloys, Seebeck coefficients were measured in a wide temperature range. Fig. 4(a)-(b) shows the Seebeck coefficients (S) and electrical resistivity of the alloys as a function of temperature, respectively. For the alloy $ZrNi_{0.5}Fe_{0.5}Sb$, initially, S is positive, indicating p-type semiconducting behavior. The Seebeck coefficient gradually rises with

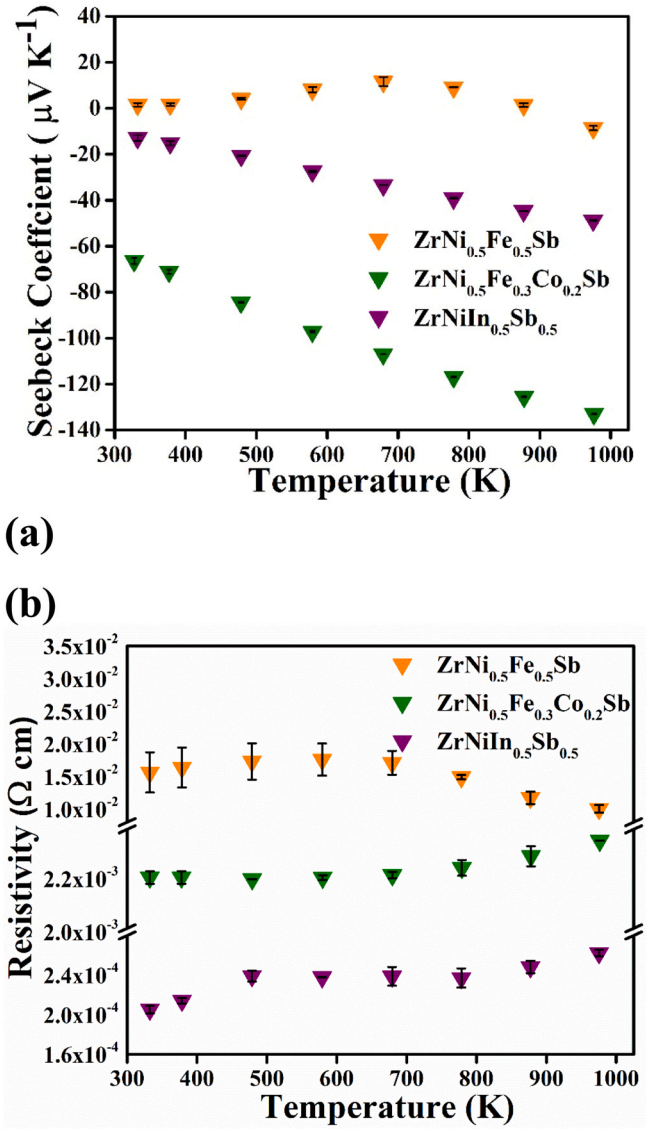

Fig. 4. Plots showing temperature dependence of (a) Seebeck coefficient, and (b) Resistivity all the half Heusler alloys.

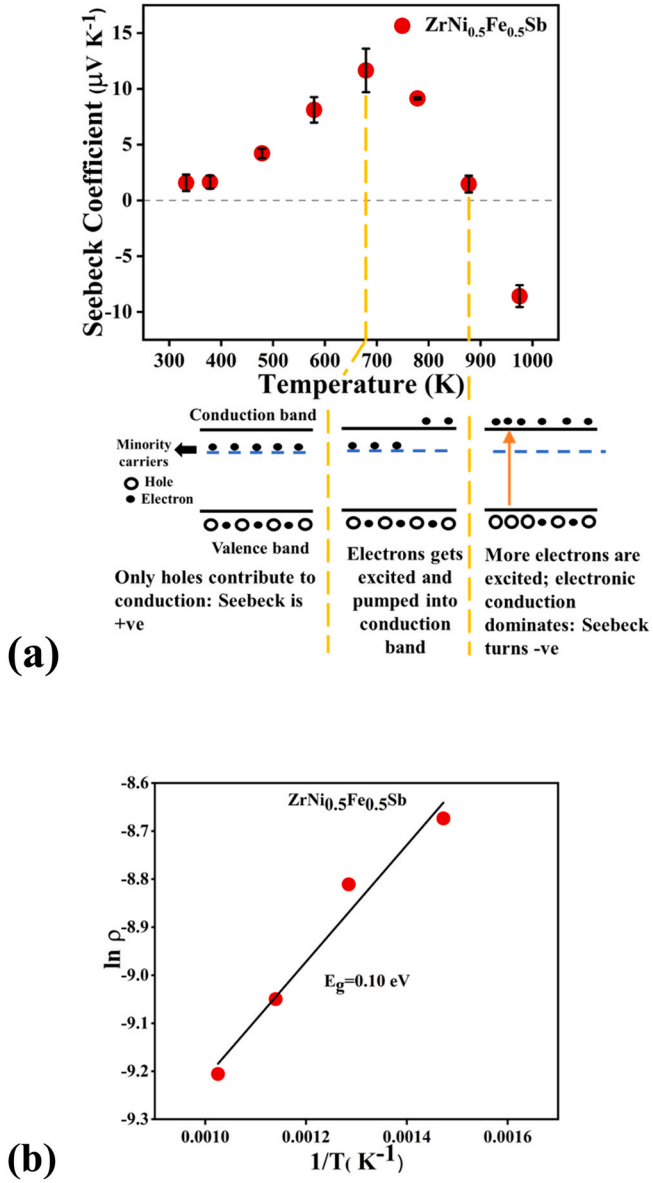

Fig. 5. (a) Schematic diagram showing the onset of bipolar conductivity; (b) Bandgap calculation from resistivity plot.

temperature till ~673 K. Thereafter, S declines with sign reversal occurring at ~888 K. To examine if such p to n type transition is occurring because of the evolution of any new phase or structural changes, DSC measurement was carried in that temperature range. No transformation peak could be detected in the DSC curve till 1073 K. The decrease in S, therefore, might be due to bipolar conduction. Similar bipolar behavior is also reported in $TiNi_{0.5}Fe_{0.5}Sb$ quaternary system [25,49]. Fig. 5(a) illustrates the effect of bipolar conduction on Seebeck coefficient as a function of temperature. The partial substitution of Co for Fe makes the alloy ZNFS-Co ($ZrNi_{0.5}Fe_{0.3}Co_{0.2}Sb$) behave as a n-type semiconductor as indicated by negative Seebeck coefficient throughout the entire range of measurement. A dramatic increase in the Seebeck coefficient was observed for ZNFS-Co alloy with a maximum value reaching − 133 μV/K at 973 K.

The Seebeck coefficient for the alloy ZNIS is negative, indicating an n-type semiconducting behavior, and it increases with temperature ruling out any bipolar conduction in this sample. In this alloy, the powder diffraction as well as the back scattered SEM microstructure indicates the phase $ZrNiIn_{0.5}Sb_{0.5}$ having the highest phase fraction, its contribution to the overall Seebeck value will also be the highest. A maximum Seebeck coefficient of − 48.7 μV/K was observed at 973 K for ZNIS. The contribution of the other impurity phases like $ZrNi_2In$, $ZrNi_{0.78}Sb_{1-x}In_x$, are smaller. It has been reported that the $ZrNi_2In$ is a metallic conductor with low resistivity at room temperature [47]. However, the type of charge carriers has not been reported so far.

As seen from Fig. 4(b), for the alloy ZNFS, there is a slight increase in ρ initially till 673 K, and then it starts to decrease with an increase in temperature. As has been observed in the temperature-dependent Seebeck coefficient, bipolar conduction commences around 673 K. Therefore, due to increase in the minority charge carriers, the overall resistivity starts to decrease on the onset of the bipolar conduction as governed by the relation, $\rho_{bipolar} = \frac{1}{n_e e\mu_e + n_p p\mu_p}$, where n_e and n_p are the concentration of electrons and holes respectively, μ_e and μ_p are the mobility of electrons and holes respectively [50]. The bandgap from the resistivity plot was estimated using Arrhenius relation $\rho \sim \exp(E_g/k_BT)$ [51]. The plot ln (ρ) as a function of (1/T) is shown in Fig. 5(b) with the slope from the linear part of the curve at lower (1/T) yield a bandgap (E_g)= 0.1 eV. For Co substituted alloy, resistivity

remains almost invariant till 700 K, after which a slight increase is observed till the end of the measurement. The overall resistivity values of Co substituted ZNFS alloy ($ZrNi_{0.5}Fe_{0.3}Co_{0.2}Sb$) are observed to be an order lower than the pristine ZNFS alloy as Co supplies an additional d-orbital electron. Therefore, substitution of Fe by Co has a positive effect on decreasing the electrical resistivity in addition to increasing the absolute Seebeck coefficient value.

The alloy ZNIS, in both the lower temperature regime (300–500 K) as well as in the high-temperature regime (800–1000 K), exhibit an increase in resistivity with temperature, indicating a metal-like behavior. In the intermediate range (500–800 K), the value remains largely constant. Since multiple phases are contributing to overall transport property, such behavior is the outcome of an interplay among various charge carrier mechanisms operating at different temperature regimes in these phases.

4. Conclusions

This study reports two new quaternary Zr-based half Heusler(hH) alloy systems $ZiNi_{0.5}Fe_{0.5}Sb$, and $ZiNiIn_{0.5}Sb_{0.5}$ having space group $F\bar{4}3m$ with lattice parameters of 0.6091 nm and 0.6104 nm, respectively. Their structural and electronic properties are evaluated. Following are the important conclusions drawn from this study.

1. The hH quarternary alloys are designed by appropriate valence balanced aliovalent substitutions, by combining ternary systems ZrNiSb having VEC of 19 with ZrXSb (X═Fe or In) having VEC of 17 to yield quaternary compounds with effective VEC of 18. A simple arc melting and consequent annealing route was adopted for the alloy synthesis. Microalloying $ZrNi_{0.5}Fe_{0.5}Sb$ with Co preserve the hH cubic crystal (Lattice parameter 0.6071 nm) structure demonstrating the possibility of tuning the system for getting desirable properties.
2. The structural characterizations through Rietveld refinements and electron diffraction pattern analyses confirm the absence of long-range ordering arising out of aliovalent substitutions carried out at various lattice sites (4c in $ZrNi_{0.5}Fe_{0.5}Sb$, $ZrNi_{0.5}Fe_{0.3}Co_{0.2}Sb$; 4b in $ZrNiIn_{0.5}Sb_{0.5}$). Additionally, no indications of any kinds of anti-site defects could be found.
3. $ZrNi_{0.5}Fe_{0.5}Sb$ exhibits p-type conduction at lower temperatures with a reversal of Seebeck sign owning to bipolar conduction at around 888 K. Upon substituting a part of the Fe sites of $ZrNi_{0.5}Fe_{0.5}Sb$ with Co having a nominal composition, $ZrNi_{0.5}Fe_{0.3}Co_{0.2}Sb$, the bipolar conductivity could be suppressed, making it n-type with a maximum Seebeck coefficient value of − 133 μV/K at 973 K. However, the $ZrNiSb_{0.5}In_{0.5}$ alloy displays an n-type behavior in the entire temperature range of measurements (room temperature to 973 K). The specific site aliovalent substitutions, therefore, can be used as an effective designing tool for tuning electronic property.
4. Simultaneous enhancement of electrical conductivity and Seebeck coefficient values of $ZrNi_{0.5}Fe_{0.3}Co_{0.2}Sb$ alloy makes it a suitable candidate for thermoelectric applications in mid-high temperature range. Furthermore, since $ZrNi_{0.5}Fe_{0.5}Sb$ is a novel quaternary half-Heusler system it can be taken up for thermoelectric material development employing strategies such as heavy doping and band gap engineering to suppress bipolar conductivity.

CRediT authorship contribution statement

Dipanjan Kumar: Conceptualization: lead, Methodology: lead, Investigation: lead, Data curation: lead, Validation: lead, Formal analysis: lead, Writing – original draft: lead, Supervision: lead. **Surafel Shiferaw Legese:** Conceptualization: Supporting, Methodology: Equal, Investigation: Equal, Data curation: Equal, Validation: equal, Formal analysis: Supporting, Writing – review & editing: supporting, Supervision: Supporting. **Shriparna Mukherjee:** Methodology: Equal, Investigation: Equal, Data curation: Equal, Validation: Equal, Formal analysis: Supporting, Writing – original draft: Supporting, Writing – review & editing: Equal, Supervision: Supporting. **Olu Emmanuel Femi:** Formal analysis: Supporting, Supervision: Supportive, Writing – review & editing: Equal. **Ravishankar Narayanan:** Formal analysis: Supporting, Supervision: Supportive, Writing – review & editing: Equal.

Declaration of Competing Interest

The authors declare that they have no known competing financial interests or personal relationships that could have appeared to influence the work reported in this paper.

Acknowledgements

The authors would like to thank the staff of Advanced facility of Microscopy and Microanalysis, AFMM. Surafel Shiferaw Legese is grateful to Jimma Institute of Technology, Jimma, Ethiopia, for a Master's scholarship and Office of International Relations (OIR), IISc for support. Olu Emmanuel Femi would also like to acknowledge the office of International relations (OIR), IISc, Bangalore, India, for accommodation support. One of the author (KC) acknowledge the support of the SERB in the form of a Distinguish Fellowship that have supported this work.

Appendix A. Supporting information

Supplementary data associated with this article can be found in the online version at doi:10.1016/j.jallcom.2022.164604.

References

[1] V. Alijani, J. Winterlik, G.H. Fecher, S.S. Naghavi, C. Felser, Quaternary half-metallic Heusler ferromagnets for spintronics applications, Phys. Rev. B 83 (2011) 184428, https://doi.org/10.1103/PhysRevB.83.184428
[2] L. Bainsla, K.G. Suresh, Equiatomic quaternary Heusler alloys: a material perspective for spintronic applications, Appl. Phys. Rev. 3 (2016) 031101, https://doi.org/10.1063/1.4959093
[3] C.J. Palmstrøm, Heusler compounds and spintronics, Prog. Cryst. Growth Charact. Mater. 62 (2016) 371–397, https://doi.org/10.1016/j.pcrysgrow.2016.04.020
[4] M. Dzero, K. Sun, V. Galitski, P. Coleman, Topological kondo insulators, Phys. Rev. Lett. 104 (2010) 106408, https://doi.org/10.1103/PhysRevLett.104.106408
[5] G. Goll, M. Marz, A. Hamann, T. Tomanic, K. Grube, T. Yoshino, T. Takabatake, Thermodynamic and transport properties of the non-centrosymmetric superconductor LaBiPt, Phys. B Condens. Matter 403 (2008) 1065–1067, https://doi.org/10.1016/j.physb.2007.10.089
[6] A. Beleanu, M. Mondeshki, Q. Juan, F. Casper, C. Felser, F. Porcher, Systematical, experimental investigations on LiMgZ(Z= P, As, Sb) wide band gap semiconductors, J. Phys. Appl. Phys. 44 (2011) 475302, https://doi.org/10.1088/0022-3727/44/47/475302
[7] D. Kieven, R. Klenk, S. Naghavi, C. Felser, T. Gruhn, I-II-V half-Heusler compounds for optoelectronics: Ab initio calculations, Phys. Rev. B 81 (2010) 075208, https://doi.org/10.1103/PhysRevB.81.075208
[8] K. Kuriyama, T. Kato, T. Tanaka, Optical band gap of the filled tetrahedral semiconductor LiZnN, Phys. Rev. B. 49 (1994) 4511–4513, https://doi.org/10.1103/PhysRevB.49.4511
[9] T. Zhu, C. Fu, H. Xie, Y. Liu, X. Zhao, High efficiency Half-Heusler thermoelectric materials for energy harvesting, Adv. Energy Mater. 5 (2015) 1500588, https://doi.org/10.1002/aenm.201500588
[10] T. Zhu, Y. Liu, C. Fu, J.P. Heremans, J.G. Snyder, X. Zhao, Compromise and synergy in high-efficiency thermoelectric materials, Adv. Mater. 29 (2017), https://doi.org/10.1002/adma.201605884
[11] P.J. Webster, K.R.A. Ziebeck, 1.5.5.1 Crystallographic structure, in: H.P.J. Wijn (Ed.), Alloys and Compounds of d-Elements with Main Group Elements Part 2, Springer-Verlag, Berlin/Heidelberg, 1988, pp. 75–79, https://doi.org/10.1007/10353201_12
[12] T. Graf, C. Felser, S.S.P. Parkin, Simple rules for the understanding of Heusler compounds, Prog. Solid State Chem. 39 (2011) 1–50, https://doi.org/10.1016/j.progsolidstchem.2011.02.001

[13] W.G. Zeier, J. Schmitt, G. Hautier, U. Aydemir, Z.M. Gibbs, C. Felser, G.J. Snyder, Engineering half-Heusler thermoelectric materials using Zintl chemistry, Nat. Rev. Mater. 1 (2016), https://doi.org/10.1038/natrevmats.2016.32

[14] M. Hellenbrandt, The inorganic crystal structure database (ICSD)—present and future, Crystallogr. Rev. 10 (2004) 17–22, https://doi.org/10.1080/08893110410001664882

[15] R. Gautier, X. Zhang, L. Hu, L. Yu, Y. Lin, T.O.L. Sunde, D. Chon, K.R. Poeppelmeier, A. Zunger, Prediction and accelerated laboratory discovery of previously unknown 18-electron ABX compounds, Nat. Chem. 7 (2015) 308–316, https://doi.org/10.1038/nchem.2207

[16] K. Xia, Y. Liu, S. Anand, G.J. Snyder, J. Xin, J. Yu, X. Zhao, T. Zhu, Enhanced thermoelectric performance in 18-Electron Nb $_{0.8}$ CoSb Half-Heusler compound with intrinsic Nb vacancies, Adv. Funct. Mater. 28 (2018) 1705845, https://doi.org/10.1002/adfm.201705845

[17] N. Naghibolashrafi, S. Keshavarz, V.I. Hegde, A. Gupta, W.H. Butler, J. Romero, K. Munira, P. LeClair, D. Mazumdar, J. Ma, A.W. Ghosh, C. Wolverton, Synthesis and characterization of Fe-Ti-Sb intermetallic compounds: discovery of a new Slater-Pauling phase, Phys. Rev. B. 93 (2016) 104424, https://doi.org/10.1103/PhysRevB.93.104424

[18] C.B.H. Evers, C.G. Richter, K. Hartjes, W. Jeitschko, Ternary transition metal antimonides and bismuthides with MgAgAs-type and filled NiAs-type structure, J. Alloy. Compd. 1–2 (1997) 93–97.

[19] H. Hohl, A.P. Ramirez, C. Goldmann, G. Ernst, B. Wölfing, E. Bucher, New compounds with MgAgAs-type structure: NbIrSn and NbIrSb, J. Phys. Condens. Matter 10 (1998) 7843–7850, https://doi.org/10.1088/0953-8984/10/35/016

[20] L. Huang, R. He, S. Chen, H. Zhang, K. Dahal, H. Zhou, H. Wang, Q. Zhang, Z. Ren, A new n-type half-Heusler thermoelectric material NbCoSb, Mater. Res. Bull. 70 (2015) 773–778, https://doi.org/10.1016/j.materresbull.2015.06.022

[21] K. Xia, Y. Liu, S. Anand, G.J. Snyder, J. Xin, J. Yu, X. Zhao, T. Zhu, Enhanced thermoelectric performance in 18-Electron Nb0.8CoSb Half-Heusler compound with intrinsic Nb vacancies, Adv. Funct. Mater. 28 (2018) 1705845, https://doi.org/10.1002/adfm.201705845

[22] W.G. Zeier, S. Anand, L. Huang, R. He, H. Zhang, Z. Ren, C. Wolverton, G.J. Snyder, Using the 18-electron rule to understand the nominal 19-electron Half-Heusler NbCoSb with Nb vacancies, Chem. Mater. 29 (2017) 1210–1217, https://doi.org/10.1021/acs.chemmater.6b04583

[23] S. Anand, M. Wood, Y. Xia, C. Wolverton, G.J. Snyder, Double Half-Heuslers, Joule 3 (2019) 1226–1238, https://doi.org/10.1016/j.joule.2019.04.003

[24] New phases of MgAgAs , LiGaGe and TiNiSi structural types containing d- and p-elements; Novye fazy strukturnykh tipov MgAgAs, LiGaGe i TiNiSi, soderzhashchie d- i p-ehlementy (Journal Article) | ETDEWEB, (n.d.). ⟨https://www.osti.gov/etdeweb/biblio/20077647⟩ (Accessed 23 May 2020).

[25] Z. Liu, S. Guo, Y. Wu, J. Mao, Q. Zhu, H. Zhu, Y. Pei, J. Sui, Y. Zhang, Z. Ren, Design of high-performance disordered Half-Heusler thermoelectric materials using 18-electron rule, Adv. Funct. Mater. 29 (2019) 1905044, https://doi.org/10.1002/adfm.201905044

[26] N. Naghibolashrafi, S. Keshavarz, V.I. Hegde, A. Gupta, W.H. Butler, J. Romero, K. Munira, P. LeClair, D. Mazumdar, J. Ma, A.W. Ghosh, C. Wolverton, Synthesis and characterization of Fe-Ti-Sb intermetallic compounds: discovery of a new Slater-Pauling phase, Phys. Rev. B 93 (2016) 104424, https://doi.org/10.1103/PhysRevB.93.104424

[27] A. Tavassoli, A. Grytsiv, G. Rogl, V.V. Romaka, H. Michor, M. Reissner, E. Bauer, M. Zehetbauer, P. Rogl, The half Heusler system Ti $_{1+x}$ Fe $_{1.33-x}$ Sb–TiCoSb with Sb/Sn substitution: phase relations, crystal structures and thermoelectric properties, Dalton Trans. 47 (2018) 879–897, https://doi.org/10.1039/C7DT03787B

[28] V.V. Romaka, P. Rogl, L. Romaka, Yu Stadnyk, N. Melnychenko, A. Grytsiv, M. Falmbigl, N. Skryabina, Phase equilibria, formation, crystal and electronic structure of ternary compounds in Ti–Ni–Sn and Ti–Ni–Sb ternary systems, J. Solid State Chem. 197 (2013) 103–112, https://doi.org/10.1016/j.jssc.2012.08.023

[29] L. Romaka, A. Tkachuk, Yu Stadnyk, V.A. Romaka, Phase equilibria in Zr–Ni–Sb ternary system at 870K, J. Alloy. Compd. 470 (2009) 233–236, https://doi.org/10.1016/j.jallcom.2008.03.030

[30] G. Melnyk, A. Leithe-Jasper, P. Rogl, R. Skolozdra, The antimony-iron-zirconium (Sb-Fe-Zr) system, J. Phase Equilib. 20 (1999) 497–507, https://doi.org/10.1361/105497199770340752

[31] H. Kleinke, C. Felser, Differences and similarities between the isotypic antimonidesMFe1−xSb, ScCo1−xSb, andMNiSb (M=Zr, Hf), J. Solid State Chem. 144 (1999) 330–338, https://doi.org/10.1006/jssc.1999.8157

[32] N.S. Chauhan, S. Bathula, B. Gahtori, Y.V. Kolen'ko, A. Dhar, Enhanced thermoelectric performance in Hf-Free p-Type (Ti, Zr)CoSb Half-Heusler alloys, J. Electron. Mater. 48 (2019) 6700–6709, https://doi.org/10.1007/s11664-019-07486-y

[33] S. Liu, Y. Hu, S. Dai, Z. Dong, G. Wu, J. Yang, J. Luo, Synergistically optimizing electrical and thermal transport properties of ZrCoSb through Ru doping, ACS Appl. Energy Mater. 4 (2021) 13997–14003, https://doi.org/10.1021/acsaem.1c02802

[34] C.B. Alcock, V.P. Itkin, M.K. Horrigan, Vapour pressure equations for the metallic elements: 298–2500K, Can. Metall. Q. 23 (1984) 309–313, https://doi.org/10.1179/cmq.1984.23.3.309

[35] V. Zaremba, D. Kaczorowski, L.D. Gulaj, Ya.M. Kalychak, J. Stepien-Damm, Crystal structure, magnetic and electrical properties of ZrNi2In and ZrCu2In, J. Alloy. Compd. 292 (1999) 1–3, https://doi.org/10.1016/S0925-8388(99)00083-3

[36] R. Pöttgen, R. Dronskowski, Structure and properties of Zr2Ni2In and Zr2Ni2Sn, J. Solid State Chem. 128 (1997) 289–294, https://doi.org/10.1006/jssc.1996.7224

[37] (ϒ), M. Kalychak, V.I. Zaremba, V.M. Baranyak, V.K. Pecharsky, Crystal structure of zirconium nickel indium (2/1/5), Zr2NiIn5, Z. Krist. Cryst. Mater. 205 (1993) 335–336, https://doi.org/10.1524/zkri.1993.205.12.335

[38] S. Kirklin, J.E. Saal, B. Meredig, A. Thompson, J.W. Doak, M. Aykol, S. Rühl, C. Wolverton, The open quantum materials database (OQMD): assessing the accuracy of DFT formation energies, npj Comput. Mater. 1 (2015) 1–15, https://doi.org/10.1038/npjcompumats.2015.10

[39] J.E. Saal, S. Kirklin, M. Aykol, B. Meredig, C. Wolverton, Materials design and discovery with high-throughput density functional theory: the open quantum materials database (OQMD), JOM 65 (2013) 1501–1509, https://doi.org/10.1007/s11837-013-0755-4

[40] J. Krez, J. Schmitt, G.J. Snyder, C. Felser, W. Hermes, M. Schwind, Optimization of the carrier concentration in phase-separated half-Heusler compounds, J. Mater. Chem. A 2 (2014) 13513–13518, https://doi.org/10.1039/C4TA03000A

[41] K. Xia, P. Nan, S. Tan, Y. Wang, B. Ge, W. Zhang, S. Anand, X. Zhao, G.J. Snyder, T. Zhu, Short-range order in defective half-Heusler thermoelectric crystals, Energy Environ. Sci. 12 (2019) 1568–1574, https://doi.org/10.1039/C8EE03654C

[42] J.E. Douglas, P.A. Chater, C.M. Brown, T.M. Pollock, R. Seshadri, Nanoscale structural heterogeneity in Ni-rich half-Heusler TiNiSn, J. Appl. Phys. 116 (2014) 163514, https://doi.org/10.1063/1.4900497

[43] K. Hattori, H. Miyazaki, K. Yoshida, M. Inukai, Y. Nishino, Direct observation of the electronic structure in thermoelectric half-Heusler alloys Zr1−xMxNiSn (M = Y and Nb), J. Appl. Phys. 117 (2015) 205102, https://doi.org/10.1063/1.4921812

[44] H. Miyazaki, T. Nakano, M. Inukai, K. Soda, Y. Izumi, T. Muro, J. Kim, M. Takata, M. Matsunami, S. Kimura, Y. Nishino, Electronic and local crystal structures of the ZrNiSn Half-Heusler thermoelectric material, Mater. Trans. 55 (2014) 1209–1214, https://doi.org/10.2320/matertrans.E-M2014803

[45] J. Schmitt, Z.M. Gibbs, G. Jeffrey Snyder, C. Felser, Resolving the true band gap of ZrNiSn half-Heusler thermoelectric materials, Mater. Horiz. 2 (2015) 68–75, https://doi.org/10.1039/C4MH00142G

[46] H.-H. Xie, J.-L. Mi, L.-P. Hu, N. Lock, M. Chirstensen, C.-G. Fu, B. Brummerstedt Iversen, X.-B. Zhao, T.-J. Zhu, Interrelation between atomic switching disorder and thermoelectric properties of ZrNiSn half-Heusler compounds, CrystEngComm 14 (2012) 4467–4471, https://doi.org/10.1039/C2CE25119A

[47] V. Zaremba, D. Kaczorowski, L.D. Gulaj, Ya.M. Kalychak, J. Stepien-Damm, Crystal structure, magnetic and electrical properties of ZrNi2In and ZrCu2In, J. Alloy. Compd. 292 (1999) 1–3, https://doi.org/10.1016/S0925-8388(99)00083-3

[48] J. Edington, Interpretation of Transmission electron Micrographs, in: Pract. Electron Microsc. Mater. Sci., Van Nostrand Reinhold company, n.d.: pp. 147–157.

[49] N. Li, H. Zhu, W. He, B. Zhang, W. Cui, Z.-Y. Hu, X. Sang, X. Lu, G. Wang, X. Zhou, Realizing both n- and p-types of high thermoelectric performance in Fe 1−x Ni x TiSb half-Heusler compounds, J. Mater. Chem. C 8 (2020) 3156–3164, https://doi.org/10.1039/C9TC06318H

[50] S.M. Sze, M.K. Lee, Carrier transport phenomena, Semiconductor Devices: Physics and Technology, third ed., John Wiley & Sons INC, 2012, pp. 48–49.

[51] C. Kittel, Semiconductor crystals, Introduction to Solid State Physics, eight ed., John Wiley & Sons, 2005, pp. 205–208.